

Hybrid Tandem Quantum Dot/Organic Solar Cells with Enhanced Photocurrent and Efficiency via Ink and Interlayer Engineering

Taesoo Kim, Yuliar Firdaus, Ahmad R. Kirmani, Ru-Ze Liang, Hanlin Hu, Mengxia Liu, Abdulrahman El Labban, Sjoerd Hoogland, Pierre M. Beaujuge, Edward H. Sargent, and Aram Amassian

ACS Energy Lett., **Just Accepted Manuscript** • DOI: 10.1021/acsenergylett.8b00460 • Publication Date (Web): 03 May 2018

Downloaded from <http://pubs.acs.org> on May 10, 2018

Just Accepted

“Just Accepted” manuscripts have been peer-reviewed and accepted for publication. They are posted online prior to technical editing, formatting for publication and author proofing. The American Chemical Society provides “Just Accepted” as a service to the research community to expedite the dissemination of scientific material as soon as possible after acceptance. “Just Accepted” manuscripts appear in full in PDF format accompanied by an HTML abstract. “Just Accepted” manuscripts have been fully peer reviewed, but should not be considered the official version of record. They are citable by the Digital Object Identifier (DOI®). “Just Accepted” is an optional service offered to authors. Therefore, the “Just Accepted” Web site may not include all articles that will be published in the journal. After a manuscript is technically edited and formatted, it will be removed from the “Just Accepted” Web site and published as an ASAP article. Note that technical editing may introduce minor changes to the manuscript text and/or graphics which could affect content, and all legal disclaimers and ethical guidelines that apply to the journal pertain. ACS cannot be held responsible for errors or consequences arising from the use of information contained in these “Just Accepted” manuscripts.

1
2
3 Hybrid Tandem Quantum Dot/Organic Solar Cells with Enhanced
4
5
6 Photocurrent and Efficiency *via* Ink and Interlayer Engineering
7
8

9 Taesoo Kim,[†] Yuliar Firdaus,[†] Ahmad R. Kirmani,[†] Ru-Ze Liang,[†] Hanlin Hu,[†] Mengxia Liu,[‡]
10
11 Abdulrahman El Labban,[†] Sjoerd Hoogland,[‡] Pierre M. Beaujuge,[†] Edward H. Sargent,[‡] and
12
13 Aram Amassian^{*,†}
14
15
16
17
18

19 [†]King Abdullah University of Science and Technology (KAUST), KAUST Solar Center
20
21 (KSC), and Physical Sciences and Engineering Division, Thuwal 23955-6900, Saudi Arabia
22
23

24 [‡]Department of Electrical and Computer Engineering, University of Toronto, Toronto, Ontario
25
26 M5S 3G4, Canada
27
28
29

30
31 AUTHOR INFORMATION
32

33 **Corresponding Author**
34

35 *E-mail: aram.amassian@kaust.edu.sa. Phone: +966 12 808 4470
36
37

38 Notes
39

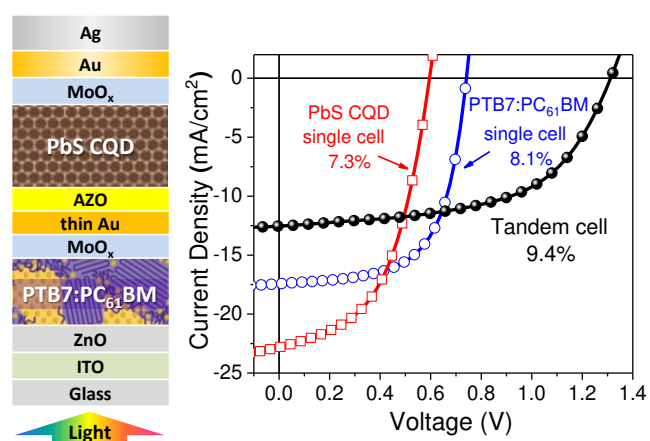
40 The authors declare no competing financial interest.
41
42
43
44

45 **ABSTRACT**
46
47

48 Realization of colloidal quantum dot (CQD)/organic photovoltaic (OPV) tandem solar
49
50 cells that integrate the strong infrared absorption of CQDs with large photovoltages of OPVs
51
52 is an attractive option toward high-performing, low-cost thin film solar cells. To date,
53
54 monolithic hybrid tandem integration of CQD/OPV solar cells has been restricted due to the
55
56 CQD ink's catastrophic damage to the organic subcell, thus forcing the low bandgap CQD to
57
58 be used as front cell. This sub-optimal configuration limits the maximum achievable
59
60

1
2
3 photocurrent in CQD/OPV hybrid tandem solar cells. In this work, we demonstrate hybrid
4 tandem solar cells employing a low-bandgap CQD back cell on top of an organic front cell
5 thanks to a modified CQD ink formulation and a robust interconnection layer (ICL) which
6 together overcome the long-standing integration challenges for CQD and organic subcells. The
7 resulting tandem architecture surpasses previously reported current densities by ~20-25% and
8 yields a state-of-the-art power conversion efficiency (PCE) of 9.4%.

18 TOC GRAPHICS



39
40 Organic and colloidal quantum dot (CQD) light absorbers are attractive solution-
41 processed materials for thin film photovoltaics (PV), enabling roll-to-roll manufacturing of
42 cost-effective lightweight modules at low temperature.¹⁻⁸ Individual materials are currently
43 limited to ca. 13% certified power conversion efficiency (PCE) in single-junction solar cells.⁹⁻
44
45
46
47
48
49
50
51
52
53
54
55
56
57
58
59
60
12 Multi-junction solar cell architectures can harvest a larger portion of the solar spectrum.¹³⁻¹⁹
CQD solids benefit from a size-tunable bandgap that allows absorbing a wide range of
wavelengths from visible to near infrared.^{4-8,11} Meanwhile, organic absorbers tend to have a
narrower spectral absorption compared to quantum dot solids,^{1,2,9,10,20} making them especially
attractive for multi-junction CQD and organic solar cells, especially if materials are selected to

1
2
3 exhibit complementary light absorption properties. In recent years, CQD/organic hybrid
4 tandem solar cells have been monolithically integrated and reported by several groups.²¹⁻²⁶
5
6 However, one noteworthy limitation in all the reports has been the unusual placement of the
7
8 low bandgap CQD subcell as the front cell, namely on the transparent electrode-coated glass
9
10 substrate, limiting the ability of the tandem to generate higher photocurrent. The primary reason
11
12 constraining researchers to this architecture is the incompatibility of the CQD ink solvents with
13
14 underlayers, including the bulk heterojunction (BHJ) organic photoactive layer and the
15
16 interconnection layers (ICL).²²⁻²⁵ The secondary, yet still important reason, is the need for
17
18 repeated solid state ligand exchange in many legacy recipes for CQD active layer or for the
19
20 CQD hole transporting layer (HTL).^{4,5,8,11} Ligand exchange, which significantly densifies the
21
22 CQD film, has been shown to cause additional chemical damage and stress-induced cracking
23
24 of underlayers.²²⁻²⁴ Tong *et al.* have suggested top-illumination in CQD/organic hybrid tandem
25
26 solar cells using transparent indium-doped tin oxide (ITO) bottom and PEDOT:PSS top
27
28 electrodes, respectively.²⁴ However, illuminating from the top still resulted in poorly
29
30 performing devices, since the illumination direction strongly affects the light harvesting by the
31
32 depleted heterojunction (DHJ) CQD subcell.^{27,28} This favors illumination through the n-type
33
34 electron transporting layer (ETL), which is typically at the bottom of n-p and n-i-p CQD solar
35
36 cells, placing additional constraints on the subcell and hybrid tandem configurations. We have
37
38 taken the view that overcoming these challenges and successfully integrating solution-
39
40 processed low bandgap CQD solar cells on top of the organic front cell is crucial to realize
41
42 highly efficient tandem solar cells which surpass the performances of state-of-the-art single-
43
44 junction CQD or organic solar cells. Indeed, two-terminal hybrid tandem solar cells are
45
46 predicted to achieve a 30% higher photocurrent for the same active materials simply by
47
48 switching the CQD subcell to the back and placing the OPV subcell at the front (**Figure 1**).
49
50
51
52
53
54
55
56
57
58
59
60

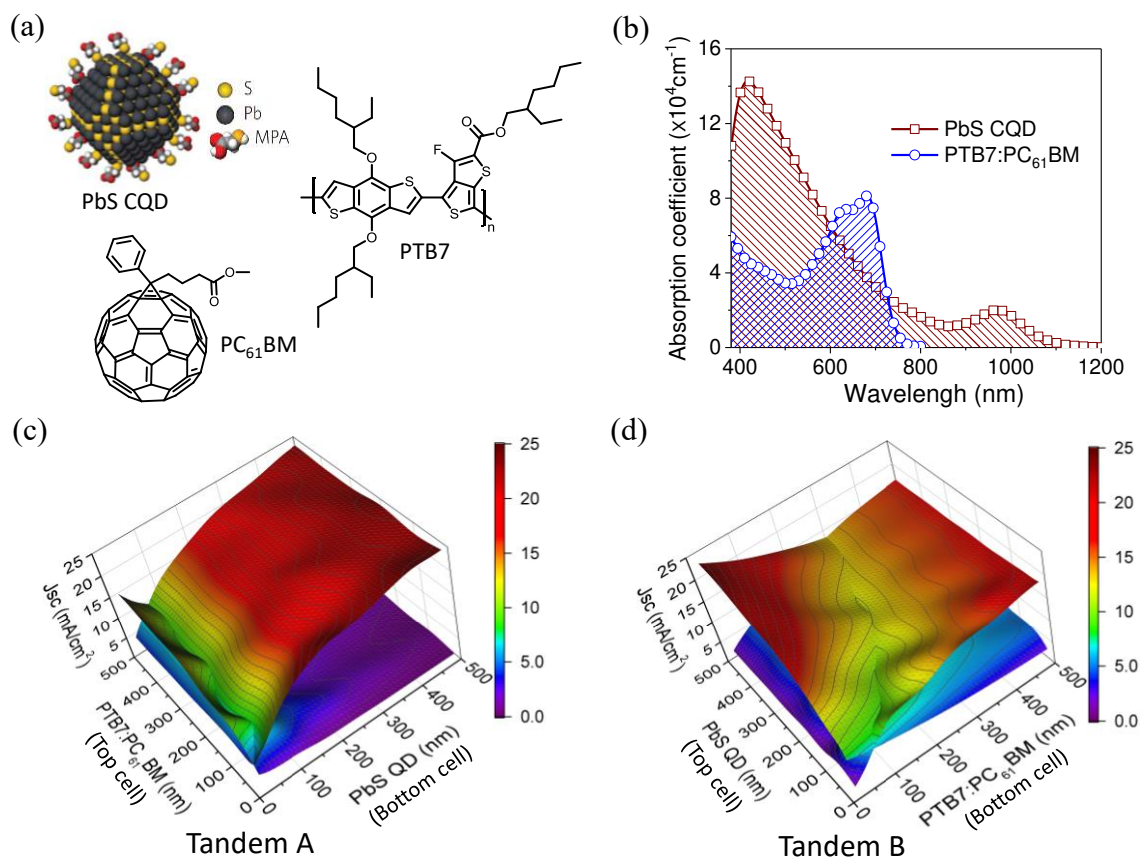


Figure 1. (a) Materials chart: PbS quantum dots after ligand exchange, the polymer donor PTB7 and the fullerene acceptor PC₆₁BM. (b) Absorption coefficients of the PbS CQD and the PTB7:PC₆₁BM active layers. (c) Simulated J_{SC} of the hybrid tandem solar cells depending on the device structures: (c) PbS CQD active layer as front cell, while organic active layer as back cell (Tandem A), (d) PbS CQD active layer as back cell, while organic active layer as front cell (Tandem B). The cross-matched intersection of the surface plot shows the current matched values achievable in each case, giving a 30% advantage to Tandem B. The contour is drawn with 1 mA/cm² increments.

In this letter, we successfully overcome the challenges of monolithic integration of a low bandgap CQD subcell directly on top of a high bandgap organic front cell to achieve state-of-the-art PCE for hybrid tandem CQD/OPV solar cells by experimentally achieving a 20-25% increase of the photocurrent as compared to the previously reported values to date.^{21-23, 25,26} To do so, we have designed a modified CQD ink formulation and a robust electrical ICL which

1
2
3 are compatible and preserve the integrity of the underlying OPV front cell. The reformulated
4 CQD ink utilizes hexane,²⁵ which reduces damage to the delicate organic BHJ layer and cuts
5 the number of steps required for CQD layer deposition, better preserving the integrity of all
6 underlayers, including the ICL. The tandem's open circuit voltage (V_{OC}) of 1.31 V is equal to
7 the sum of subcell voltages, while the photocurrent of 12.5 mA/cm² and the PCE of 9.4% are
8 the highest reported to date in CQD/organic hybrid tandem solar cells.²¹⁻²⁶ The tandem PCE
9 significantly surpasses those of the organic (8.1%) and CQD (7.3%) subcells, highlighting the
10 success of the integration approach. This successful demonstration is an important milestone
11 for the monolithic integration of state-of-the-art CQD and organic solar cells into tandem
12 devices that can outperform the best single-junction solar cells in each field.
13
14
15
16
17
18
19
20
21
22
23
24
25

26 In **Figure 1(a)** we show the material systems used in this study: the chemical structures
27 of the polymer donor, thieno[3,4-b]thiophene/benzodithiophene (PTB7), and fullerene
28 acceptor, [6,6]-phenyl-C₆₀-butyric acid methyl ester (PC₆₁BM),²⁹⁻³¹ as well as a PbS CQD with
29 an organic 3-mercaptopropionic acid (MPA) ligand.^{32,33} The high-resolution transmission
30 electron microscopy (TEM) image of PbS CQDs before ligand exchange is shown in **Figure**
31 **S1** (average CQD size: ~ 3.5 nm). PTB7 was used in conjunction with PC₆₁BM to form the
32 polymer:fullerene organic bulk heterojunction subcell. The absorption coefficients of the
33 PTB7:PC₆₁BM and PbS CQD active layers are shown in **Figure 1(b)**. The CQD layer shows
34 relatively strong absorption in the short-wavelength visible range and weaker absorption in the
35 red and NIR with an exciton peak at 970 nm, while the PTB7:PC₆₁BM subcell transmits, to
36 some extent, the visible spectrum at around 500 nm and then absorbs effectively in the red
37 regions (up to 750 nm), compensating for the CQD layer's weaker absorption in the red regions.
38 The spectral responses of the two active layers are thus reasonably complementary.²⁵
39
40
41
42
43
44
45
46
47
48
49
50
51
52
53
54
55

56 In previous reports on CQD/organic hybrid tandem solar cells, the device architectures
57 have been configured such that the CQD subcell is located at the bottom on the transparent
58
59
60

1
2
3 substrate, while the organic subcell is fabricated above.²¹⁻²⁶ This forces the incident light to be
4 absorbed first by the low bandgap CQD layer with the remaining light transmitted through the
5 ICL, and then absorbed by the organic active layer.^{21-23,25,26} Importantly, the J_{SC} of the tandem
6 device is limited in this configuration, despite the partial spectral complementarity of the active
7 layers, limiting, in turn, the achievable PCE by the tandem as compared to the individual CQD
8 and organic single-junction cells. Optical simulations were performed to compare the two
9 CQD/organic hybrid tandem architectures, with tandem A (**Figure S2(a)**) placing the CQD
10 subcell at the bottom side,^{22,23,25,26} and tandem B (**Figure S2(b)**) placing it at the top side. The
11 device structures, layer thicknesses, and optical constants are depicted in **Figure S2**. The
12 simulated current densities of tandem A and B are shown in **Figure 1(c)** and **1(d)**, respectively,
13 for active layer thicknesses ranging from 0 to 500 nm, with light incidence from the glass
14 substrate side in both scenarios. The simulations predict a J_{SC} as high as ca. 10 mA/cm² for
15 tandem A and ca. 13 mA/cm² for tandem B, and identify optimal subcell thicknesses for these
16 scenarios, clearly showing a 30% advantage for tandem B. Hence, the complementary
17 absorption by the two active layers is more effective in tandem B than in tandem A. The ca.
18 30% advantage of tandem B in terms of in J_{SC} motivates its fabrication, but poses serious
19 challenges from the monolithic integration perspective. In particular, the bottom organic active
20 layer is easily dissolved or damaged by some of the solvents typically used for CQD coating
21 and/or ligand exchange, imposing important restrictions on the CQD ink and its coating
22 process.²¹⁻²⁶ We have set out to investigate alternative CQD ink solvents and robust ICLs which
23 can survive the CQD coating process and provide protection for all underlayers.
24
25
26
27
28
29
30
31
32
33
34
35
36
37
38
39
40
41
42
43
44
45
46
47
48
49
50
51
52
53
54
55
56
57
58
59
60

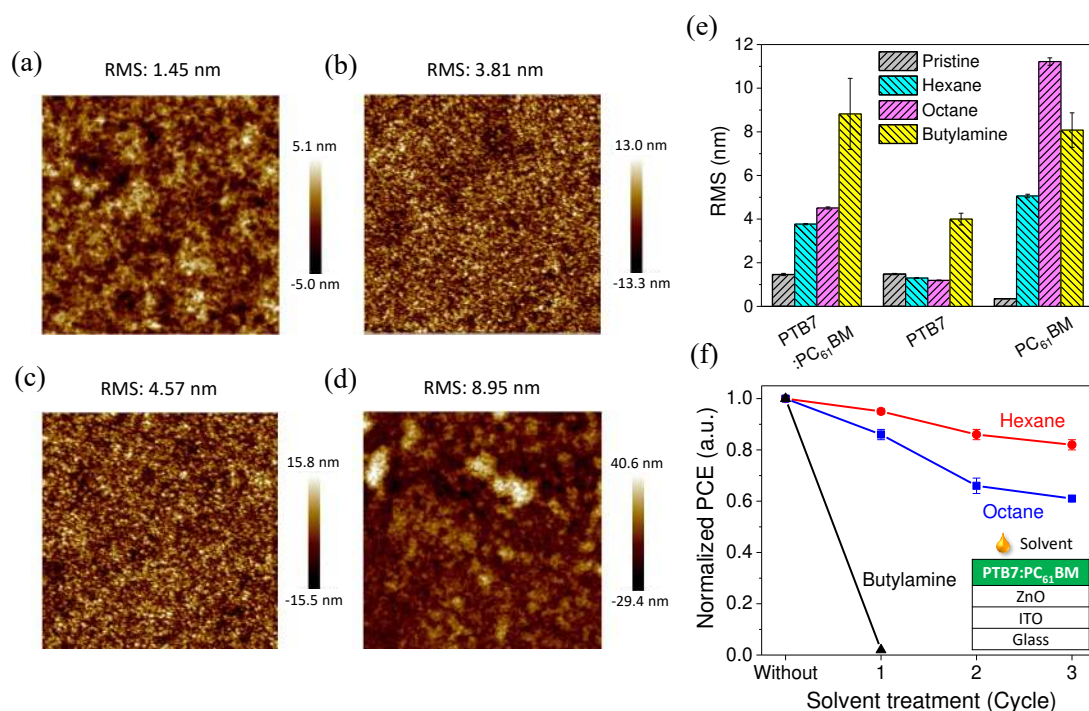


Figure 2. AFM images of PTB7:PC₆₁BM surface topography, (a) before the solvent treatment, treated with (b) hexane, (c) octane, and (d) butylamine, respectively. The scan size is 5 μm x 5 μm . (e) Summary of RMS surface roughness of solvent-treated organic thin films of PTB7:PC₆₁BM, only PTB7, and only PC₆₁BM, respectively. (f) Normalized PCE of organic single-junction cells without and with direct solvent-treatment of the photoactive layers (without a protective ICL).

Octane and butylamine are the two most commonly used solvents for conventional PbS CQD solar cells.^{4-8,11,25,32,33} In **Figure 2**, we investigate and compare the effects of exposure to the two common CQD solvents (octane and butylamine) on the morphology of the organic BHJ layer and the operational stability of a single-junction organic solar cell. For this purpose, we have exposed the PTB7:PC₆₁BM BHJ layers directly to blank solvents, which were cast and spun off of the organic photoactive layers in a manner which simulates CQD coating conditions. The solvent treatments were performed in the absence of the ICL in order to simulate the worst case scenario of solvent damage. We assess the solvent effects on BHJ morphology by performing atomic force microscopy (AFM) measurements of the surface

1
2
3 topography before and after exposure to each solvent. We subsequently fabricated single-
4
5 junction organic solar cells using similarly solvent-treated photoactive layers (see experimental
6
7 section of supporting information about the solvent treatment method). In **Figure 2(a)** we see
8
9 AFM images of the surface morphology of an as-prepared PTB7:PC₆₁BM active layer,
10
11 exhibiting a root mean squared (RMS) roughness of 1.45 nm. Micrographs in **Figures 2(b, c,**
12
13 **d)** show that the BHJ layer roughens moderately in the case of octane and very significantly in
14
15 the case of butylamine, indicative of significant solvent-BHJ interactions. We summarize in
16
17 **Figure 2(e)**, the RMS surface roughness of pristine PTB7, PC₆₁BM, and PTB7:PC₆₁BM blend
18
19 layers and after solvent treatment. AFM images of PTB7 and PC₆₁BM before and after solvent
20
21 treatment are presented in **Figure S3**. The data attribute the increasing RMS roughness of the
22
23 PTB7:PC₆₁BM blend to partial solubility of PC₆₁BM in octane, whereas butylamine dissolves
24
25 both the PTB7 and PC₆₁BM.
26
27
28
29

30
31 These changes to the active layer's morphology understandably impact the operation
32
33 of organic solar cells. We plot the normalized PCE of the solvent-treated PTB7:PC₆₁BM single-
34
35 junction cells with respect to the number of solvent treatments in **Figure 2(f)**. A one-time
36
37 exposure to butylamine is sufficient to render the solar cell inoperable, whereas octane
38
39 exposure is less invasive, but reduces efficiency by 40% after three treatments. Even when
40
41 butylamine solvent treatment was applied indirectly through the ICL (see below for detailed
42
43 selection criteria of ICL) in a simulated solar cell stack (glass/ITO/PTB7:PC₆₁BM/MoO_x/thin
44
45 Au/AZO) (**Figure S4(b-c)**) it caused significant damage by dissolving the organic layer.
46
47 Octane had a far less dramatic, but non-negligible effect. Fortunately, 3-mercaptopropionic
48
49 acid (MPA) in acetonitrile (ACN) treatment used to simulate the CQD ligand exchange did not
50
51 show negative effect on organic device performance (**Figure S4(a)**).³³ We therefore conclude
52
53 that the latest, most modern CQD inks based on butylamine are particularly difficult to apply
54
55 at this stage in the tandem B architecture, with octane emerging as a better choice, but one
56
57
58
59
60

1
2
3 which is still unacceptable since it reduces the operational performance of the OPV subcell
4 through the protective ICL.
5
6

7
8 Addressing these issues requires a solvent which can disperse CQDs and minimize
9 harmful interactions with the underlying OPV subcell and the ICL. We propose hexane as an
10 alternative solvent since it is considered a marginal solvent for many organic semiconductors.
11 Hexane also has the advantage of a much lower boiling point (68 °C) than octane (125 °C),
12 allowing it to dry much faster and minimize liquid-OPV interactions during CQD spin-coating.
13
14 Indeed, we show in **Figure 2** that hexane appears to induce the smallest morphological changes
15 to the organic photoactive layer among all three solvents. Hexane is also found to have minimal
16 effect on the ICL compared to octane and butylamine (**Figure S4(b-d)**). Importantly, hexane
17 exposure shows the smallest loss on OPV devices, with a 5% drop in PCE after a single direct
18 treatment and 20% drop in PCE after three cycles of solvent treatment. These losses should be
19 mitigated further by the protective ICL.
20
21
22
23
24
25
26
27
28
29
30
31
32

33 The fast-drying solvent has an additional mitigating benefit by reducing the number of
34 CQD coating steps. CQD films coated using octane and hexane-based inks of identical
35 concentration (50 mg/mL) result in a final CQD thickness (after MPA ligand exchange) of 40
36 nm (2500 rpm) when using octane,²² and 100 nm (3000 rpm) when using hexane. This
37 difference is ascribed to the rapid drying and solidification of the ink, which reduces the time
38 window within which the ink can be ejected during the spin-up and outflow regimes of spin-
39 coating.³⁴ The ability of hexane to decrease the number of CQD coating cycles required to
40 achieve thicker films required for the tandem B architecture can thus significantly reduce the
41 potential damage to underlayers compared to octane by a combination of reduced interaction
42 strength and interaction time. The choice of hexane forces the use of a legacy CQD DHJ top
43 cell using a hexane-based ink and MPA ligand exchange as the most suitable approach for
44 successful monolithic integration of a CQD back cell on top of the OPV front cell.
45
46
47
48
49
50
51
52
53
54
55
56
57
58
59
60

1
2
3 The design and selection of the ICL to connect the CQD back cell to the underlying
4 organic front cell was also significantly constrained by the same stringent requirements posed
5 by the CQD deposition and ligand exchange on top of the ICL and organic underlayers. These
6 constraints are as follows: (1) sensitivity to solvents used in the CQD layer deposition,^{22,24} (2)
7 sensitivity to heat as PTB7 (and many related donor materials) does not fare well under thermal
8 annealing or high temperature deposition,³⁵ and (3) sensitivity to mechanical stresses induced
9 by solid-state ligand exchange.³⁶ The low-temperature processing requirement excludes the use
10 of popular interlayers, such as sol-gel ZnO and TiO₂ as ETL and PEDOT:PSS as HTL due to
11 their thermal annealing requirements.^{13,37-40} The mechanical stress resistance requirement also
12 excludes most organic interlayers and films processed by thermal evaporation at the expense
13 of sputtering at low-temperature. However, organic semiconductors are easily damaged by
14 sputtering, requiring the first layer of the ICL in direct contact with the organic BHJ layer to
15 be vacuum-evaporated instead and be sufficiently robust to withstand subsequent sputtering.⁴¹
16 For these reasons, we have opted for a tri-layer ICL with vacuum-evaporated MoO_x on the
17 organic side and a metal oxide ETL on the CQD side.^{18,19,23,41-44} The central layer of the ICL
18 was an ultrathin (0.5 nm) Au layer which breaks up into islands acting as effective
19 recombination sites,⁴²⁻⁴⁴ as will be discussed below. We have opted for Al-doped ZnO (AZO)
20 deposited by RF-sputtering as the n-type ETL.²⁵ The conductivity of the AZO layer used here
21 was $\leq 10^{-7}$ S/cm. **Figure S5** shows the significant damage to metal oxide nanoparticle (NP)
22 layers based on solution-processed AZO and ZnO NPs instead of sputtered AZO. Therefore,
23 the compact and dense AZO produced by sputtering was preferred over solution-processed
24 nanocrystal metal oxides such as AZO, TiO₂ and ZnO, etc., as these often yield less compact
25 films which can be easily permeated by or delaminated the CQD ink and/or be harmed by the
26 mechanical stress build-up in the CQD overlayer after ligand exchange. The oleic acid capped
27 PbS CQD active layer deposited from the hexane-based formulation was ligand-exchanged
28
29
30
31
32
33
34
35
36
37
38
39
40
41
42
43
44
45
46
47
48
49
50
51
52
53
54
55
56
57
58
59
60

using a 3-mercaptopropionic acid (MPA) in acetonitrile (ACN) and was repeated until the desired thickness was reached. The tandem stack was completed by vacuum evaporation of MoO_x as HTL and Au/Ag as the anode.^{25,33}

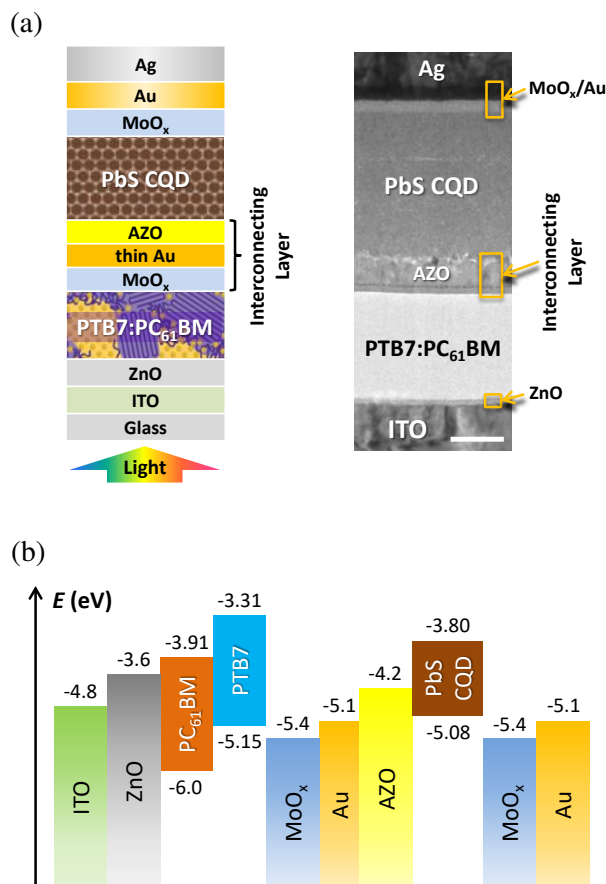


Figure 3. (a) Hybrid tandem solar cell configuration and TEM cross-sectional image of the corresponding device. Scale bar is 100 nm. (b) Energy level diagram of the hybrid tandem solar cell.

In **Figure 3(a)** we present the hybrid tandem B device schematic and show a cross-sectional transmission electron microscopy (TEM) image of the actual device based on a 200 nm thick PTB7:PC₆₁BM bottom active layer and a 300 nm PbS CQD (3 layers) active layer. The device includes a ZnO/ITO cathode, a $\text{MoO}_x/\text{Au}/\text{Ag}$ anode and the tri-layer $\text{MoO}_x/\text{thin Au}/\text{AZO}$ ICL. The energy level diagram of the hybrid tandem device is presented in **Figure 3(b)**. The PTB7:PC₆₁BM active layer was spin-cast on top of a sol-gel ZnO layer prepared by spin-coating on ITO-coated glass. The ICL consists of a stack of $\text{MoO}_x/\text{thin Au}/\text{AZO}$. MoO_x

1
2
3 was vacuum-deposited on PTB7:PC₆₁BM to form the HTL. An ultrathin Au layer (0.5 nm) was
4 deposited by thermal evaporation with careful thickness monitoring. As shown in **Figure 3(b)**,
5 the Au layer forms an asymmetric work function within the ICL which grades the work
6 function from high on the MoO_x side – to promote hole injection from the organic photoactive
7 layer into the ICL – to low work function on the AZO side – to promote electron injection from
8 the CQD photoactive layer into the ICL.^{18,19,23} The ultrathin Au layer forms nano-islands, as
9 seen in SEM and AFM measurements (**Figure S6**). These act as efficient recombination sites
10 and reduce the accumulation of photo-excited charges in the photoactive layers and near the
11 ICL.^{18,19,23,41-44} The fill factor (FF) and thus the performance of tandem cells benefits strongly
12 from the presence of Au nano-islands,^{18,19,23,25} as shown in **Figure S7(a)** of tandem solar cells
13 prepared without and with Au nano-islands within the ICL. **Figure S7(b)** compares the
14 conductance of ICL including a thin Au layer as compared to an ICL without Au and shows
15 that the inclusion of Au reduces the series resistance of the ICL.^{18,19,23,25} The device structures
16 used for conductance measurements were the isolated interlayer stacks, including
17 glass/ITO/MoO_x/Au (0.5 nm)/AZO/Al and glass/ITO/MoO_x/AZO/Al.

18
19 Individual single-junction cells were first fabricated employing organic or CQD
20 photoactive layers with different thickness using the same ETL and HTL as in the tandem B
21 architecture. The configurations for the PbS CQD and organic single cells were
22 glass/ITO/AZO/PbS CQD/MoO_x/Au/Ag and glass/ITO/ZnO/PTB7:PC₆₁BM/MoO_x/Ag,
23 respectively. In **Figure 4(a)** we show current density-voltage (*J-V*) curves obtained for CQD
24 and organic single-junction cells depending on active layer thickness ranging from 100 to 500
25 nm for the former and 145 to 210 nm for the latter. The summary of statistical device
26 parameters of the organic and CQD single-junction cells is presented in **Figures S8** and **S9**,
27 respectively, while all parameters are summarized in **Table 1**. The organic active layer
28 thickness was varied by changing the spin-coating speed, whereas the CQD active layer
29
30
31
32
33
34
35
36
37
38
39
40
41
42
43
44
45
46
47
48
49
50
51
52
53
54
55
56
57
58
59
60

1
2
3 thickness was varied by repeating the CQD coating and ligand exchange processes, which
4 incremented the thickness by 100 nm per cycle. In organic cells, increasing the active layer
5 thickness leads to higher J_{SC} at the expense of FF, with the PCE showing a small drop due to
6 the trade-off between J_{SC} and FF within the thickness range studied (**Table 1**). The single-
7 junction CQD cells also show a similar trend, with higher J_{SC} in thicker active layers with the
8 FF and PCE showing maximum values for a 300 nm thickness (**Table 1**). Looking into the V_{OC}
9 of PbS CQD single-junction cells, CQDs are known for exhibiting significant energetic losses
10 that lead to poor output voltages corresponding to the band gap. Fundamentally, the voltage
11 loss mechanism in CQDs is directly related to the significantly large number of surface atoms
12 (due to the high surface-to-volume ratio), which result in a high density of band tails. The solid-
13 state ligand exchange further enhances these band tails due to an increased morphological
14 disorder. Guyot-Sionnest has theoretically suggested that the extent of band tails currently
15 found in legacy CQD solids (obtained by solid-state ligand exchange) limits the maximum
16 achievable output voltage to 50% of the CQD band gap.⁴⁵ Therefore, ~ 0.58 V output voltage
17 for our CQD cells employing PbS CQDs with *ca.* 1.2 eV band gap is close to the theoretical
18 optimum.
19
20
21
22
23
24
25
26
27
28
29
30
31
32
33
34
35
36
37
38
39
40
41
42
43
44
45
46
47
48
49
50
51
52
53
54
55
56
57
58
59
60

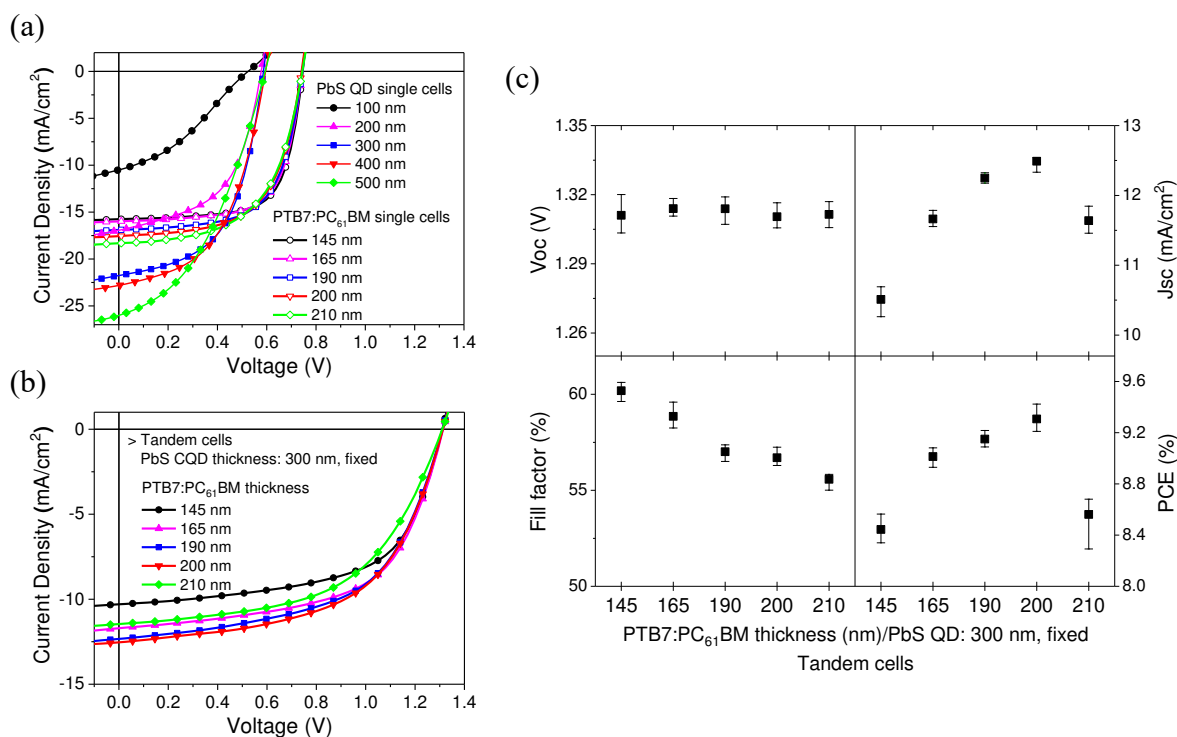


Figure 4. (a) Representative J - V curves of PTB7:PC₆₁BM, and PbS CQD single-junction cells depending on their active layer thicknesses. (b) J - V characteristics of hybrid tandem solar cells of various PTB7:PC₆₁BM layer thicknesses, fixing PbS CQD layer with 300 nm thick, and (c) statistical parameter summary of these tandem solar cells.

Table 1. Averaged device parameters of PTB7:PC₆₁BM, PbS CQD single-junction cells and hybrid tandem solar cells depending on active layer thicknesses. Average values based on 20 devices.

Device structure	Active layer	Thickness	V _{OC} (V)	J _{sc} (mA/cm ²)	FF (%)	PCE (%)	Best PCE (%)
Single cell	PTB7:PC ₆₁ BM	145 nm	0.75	15.8	69.4	8.2	8.3
		165 nm	0.75	15.9	68.1	8.1	8.2
		190 nm	0.75	16.9	64.0	8.1	8.2
		200 nm	0.74	17.4	60.8	7.9	8.1
		210 nm	0.74	18.3	58.0	7.9	8.1
	PbS CQD	100 nm	0.51	10.6	34.9	1.9	2.1
		200 nm	0.58	16.9	54.0	5.3	5.9
		300 nm	0.58	21.8	54.7	7.0	7.3
		400 nm	0.60	22.6	50.2	6.5	7.0

		500 nm	0.59	25.9	44.0	6.4	6.9
Tandem cell	PTB7:PC ₆₁ BM /PbS CQD	145 nm /300 nm	1.31	10.5	60.2	8.4	8.6
		165 nm /300 nm	1.31	11.7	58.9	9.0	9.1
		190 nm /200 nm	1.31	11.1	58.6	8.6	8.7
		190 nm /300 nm	1.31	12.3	57.0	9.2	9.2
		190 nm /400 nm	1.30	12.6	54.7	8.9	9.0
		190 nm /500 nm	1.30	12.6	53.7	8.8	8.9
		200 nm /300 nm	1.31	12.5	56.7	9.3	9.4
		210 nm /300 nm	1.31	11.6	55.6	8.6	8.7

Based on the experimental results for single-junction organic and CQD cells with re-engineered CQD ink, we have monolithically integrated CQD/organic subcells into the tandem B architecture shown in **Figure 3(a)**, namely glass/ITO/ZnO/PTB7:PC₆₁BM/MoO_x/ultrathin Au/AZO/PbS CQD/MoO_x/Au/Ag. The thicknesses of both CQD and organic active layers were varied to maximize current matching and achieve the highest PCE. Fixing the organic active layer thickness to 190 nm, the FF decreased and the J_{SC} saturated with increasing CQD active layer thickness up to 500 nm (**Figure S10, Table 1**). By contrast, fixing the CQD layer thickness to 300 nm and increasing the organic active layer thickness up to 210 nm, the FF decreased while J_{SC} peaked at a thickness of 200 nm (**Figure 4(b,c), Table 1**). Importantly, the V_{OC} was nearly constant without significant photovoltage drops, independent of either active layer thicknesses. This is significant as it indicates that the ICL and the organic subcell can survive up to five repeated CQD coating and ligand exchange steps without serious damage to the device.

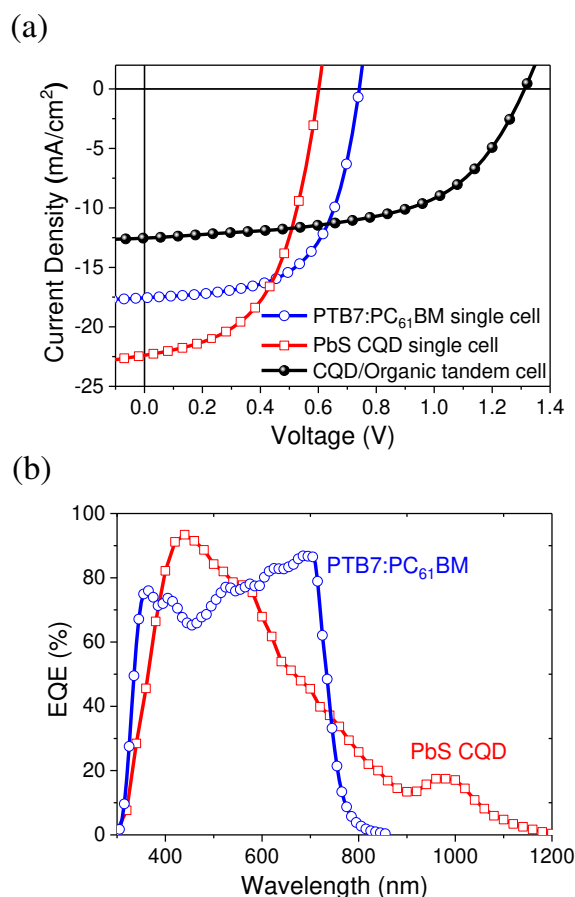


Figure 5. (a) J - V curves of optimized hybrid tandem and the single-junction cells with the same active layer thicknesses, (b) EQE spectra of the PTB7:PC₆₁BM and PbS CQD single-junction cells, which were applied for the optimized tandem cells.

The optimized hybrid tandem solar cell yielded a V_{OC} of 1.31 V, a FF of 56.7%, and a J_{SC} of 12.5 mA/cm^2 with high current matching, leading to a PCE of 9.3% on average, and a best PCE value of 9.4%. This is achieved with a 200 nm thick organic active layer and a 300 nm thick CQD active layer. The photocurrent is the highest achieved to date and surpasses by ~20-25% the previous reported photocurrent values,^{21-23,25,26} in reasonably good agreement with optical simulations reported in **Figure 1**. The shunt and series resistances of the optimized tandem and their single cells are summarized in **Table S1**.

In **Figure 5(a)** we show the J - V characteristics of single-junction and tandem cells with the same active layer thicknesses. **Figure 5(b)** shows the external quantum efficiency (EQE)

1
2
3 for the single-junction CQD and organic cells with the thickness employed in the optimized
4 tandem cell. The CQD cell harvests the solar spectrum in the short wavelength region (UV/blue
5 regions), but the EQE drops significantly from its peak at 440 nm and up to 880 nm, showing
6 a second increase at around 970 nm, corresponding to the CQD exciton peak position before
7 the band edge near 1200 nm. The EQE of the PTB7:PC₆₁BM cell is particularly pronounced
8 from the green to red region, for 500 nm < λ < 750 nm showing complementary EQE spectra
9 with CQD cell. The optimized tandem solar cells exhibit significantly higher PCE than the best
10 performing single-junction organic (8.3%) and CQD (7.1%) cells. The tandem open circuit
11 voltage (V_{OC}) of 1.31 V is equal to the sum of two single-junction cell voltages. The FF (56.7%)
12 of the optimized tandem was found to be at an intermediate level as the single-junction organic
13 (60.8%) and CQD (54.7%) cells with the same active layer thickness. These results prove that
14 the organic and CQD subcells are effectively connected and current-matched.
15
16
17
18
19
20
21
22
23
24
25
26
27
28
29
30

31 In conclusion, we demonstrated the implementation of a tandem solar cell with a
32 solution-processed PbS CQD back cell monolithically integrated through connection in series
33 with an underlying PTB7:PC₆₁BM front cell. This tandem solar cell with the CQD back cell
34 and an OPV front cell achieves higher current matching and PCE compared to previous reports.
35 The primary enabling breakthrough was the development of a CQD ink formulation which
36 minimizes chemical and structural damage to the underlying OPV subcell and ICL. The
37 secondary enabling development was the design of a robust trilayer ICL which survives the
38 chemical and mechanical stresses induced by CQD coating and ligand exchange steps whilst
39 itself not damaging the delicate organic subcell. To date, this is the most efficient CQD/organic
40 hybrid tandem structure and far exceeds the PCEs of individual subcells. This work is expected
41 to pave the way for further successful integration of hybrid tandem OPV/CQD solar cells with
42 PCE which can one day surpass the state-of-the-art PCE of each individual field.
43
44
45
46
47
48
49
50
51
52
53
54
55
56
57
58
59
60

1
2
3 ASSOCIATED CONTENT
4

5 **Supporting Information.**
6

7 Experimental methods of device fabrication, electrical characterization. AFM, TEM,
8 SEM images.
9
10
11
12

13
14 AUTHOR INFORMATION
15

16 **Corresponding author**
17

18 *E-mail: aram.amassian@kaust.edu.sa. Phone: +966 12 808 4470
19

20
21 **Notes**
22

23 The authors declare no competing financial interest.
24
25
26
27

28 ACKNOWLEDGMENT
29

30 This work was supported by the King Abdullah University of Science and Technology
31 (KAUST), and the Ontario Research Fund - Research Excellence program. M.L. acknowledges
32 support from the Hatch Research Scholarship. The authors thanks E. Palmiano for support in
33 the synthesis of quantum dots.
34
35
36
37
38
39
40
41

42 REFERENCES
43

- 44
45 (1) Heeger, A. J. 25th Anniversary Article: Bulk Heterojunction Solar Cells: Understanding
46 the Mechanism of Operation. *Adv. Mater.* **2014**, *26*, 10-28.
47
48
49 (2) Beaujuge, P. M.; Fréchet, J. M. Molecular Design and Ordering Effects in π -Functional
50 Materials for Transistor and Solar Cell Applications. *J. Am. Chem. Soc.* **2011**, *133*,
51 20009-20029.
52
53
54
55
56
57
58
59
60

- 1
2
3 (3) Finn III, M.; Martens, C. J.; Zaretski, A. V.; Roth, B.; Søndergaard, R. R.; Krebs, F. C.;
4 Lipomi, D. J. Mechanical Stability of Roll-to-Roll Printed Solar Cells under Cyclic
5 Bending and Torsion. *Solar Energy Mater. Sol. Cells* **2018**, *174*, 7-15.
6
7
8
9
10 (4) Kim, J. Y.; Voznyy, O.; Zhitomirsky, D.; Sargent, E. H. 25th Anniversary Article:
11 Colloidal Quantum Dot Materials and Devices: A Quarter-Century of Advances. *Adv.*
12 *Mater.* **2013**, *25*, 4986-5010.
13
14
15
16 (5) Wang, R.; Shang, Y.; Kanjanaboos, P.; Zhou, W.; Ning, Z.; Sargent, E. H. Colloidal
17 Quantum Dot Ligand Engineering for High Performance Solar Cells. *Energy Environ.*
18 *Sci.* **2016**, *9*, 1130-1143.
19
20
21
22
23 (6) MacDonald, B. I.; Martucci, A.; Rubanov, S.; Watkins, S. E.; Mulvaney, P.; Jasieniak, J.
24 J. Layer-by-Layer Assembly of Sintered CdSe_xTe_{1-x} Nanocrystal Solar Cells. *ACS Nano*
25 **2012**, *6*, 5995-6004.
26
27
28
29
30 (7) Crisp, R. W.; Panthani, M. G.; Rance, W. L.; Duenow, J. N.; Parilla, P. A.; Callahan, R.;
31 Dabney, M. S.; Berry, J. J.; Talapin, D. V.; Luther, J. M. Nanocrystal Grain Growth and
32 Device Architectures for High-Efficiency CdTe Ink-based Photovoltaics. *ACS Nano*
33 **2014**, *8*, 9063-9072.
34
35
36
37
38 (8) Chuang, C.-H. M.; Brown, P. R.; Bulović, V.; Bawendi, M. G. Improved Performance
39 and Stability in Quantum Dot Solar Cells through Band Alignment Engineering. *Nat.*
40 *Mater.* **2014**, *13*, 796-801.
41
42
43
44
45 (9) Li, S.; Ye, L.; Zhao, W.; Zhang, S.; Mukherjee, S.; Ade, H.; Hou, J. Energy-Level
46 Modulation of Small-Molecule Electron Acceptors to Achieve over 12% Efficiency in
47 Polymer Solar Cells. *Adv. Mater.* **2016**, *28*, 9423-9429.
48
49
50
51
52 (10) Zhao, W.; Li, S.; Yao, H.; Zhang, S.; Zhang, Y.; Yang, B.; Hou, J. Molecular
53 Optimization Enables over 13% Efficiency in Organic Solar Cells. *J. Am. Chem. Soc.*
54 **2017**, *139*, 7148-7151.
55
56
57
58
59
60

- 1
2
3 (11) Liu, M.; Voznyy, O.; Sabatini, R.; de Arquer, F. P. G.; Munir, R.; Balawi, A. H.; Lan,
4 X.; Fan, F.; Walters, G.; Kirmani, A. R.; et al. Hybrid Organic-Inorganic Inks Flatten The
5 Energy Landscape in Colloidal Quantum Dot Solids. *Nat. mater.* **2017**, *16*, 258-263.
6
7
8
9
10 (12) Sanehira, E. M.; Marshall, A. R.; Christians, J. A.; Harvey, S. P.; Ciesielski, P. N.;
11 Wheeler, L. M.; Schulz, P.; Lin, L. Y.; Beard, M. C.; Luther, J. M. Enhanced Mobility
12 CsPbI₃ Quantum Dot Arrays for Record-Efficiency, High-Voltage Photovoltaic Cells.
13 *Sci. Adv.* **2017**, *3*, eaao4204.
14
15
16
17
18 (13) Kim, J. Y.; Lee, K.; Coates, N. E.; Moses, D.; Nguyen, T.-Q.; Dante, M.; Heeger, A. J.
19 Efficient Tandem Polymer Solar Cells Fabricated by All-Solution Processing. *Science*
20 **2007**, *317*, 222-225.
21
22
23
24
25 (14) Hadipour, A.; de Boer, B.; Blom, P. W. Organic Tandem and Multi-Junction Solar Cells.
26 *Adv. Funct. Mater.* **2008**, *18*, 169-181.
27
28
29
30 (15) Li, G.; Chang, W.-H.; Yang, Y. Low-Bandgap Conjugated Polymers Enabling Solution-
31 Processable Tandem Solar Cells. *Nat. Rev. Mater.* **2017**, *2*, 17043.
32
33
34
35 (16) Cui, Y.; Yao, H.; Gao, B.; Qin, Y.; Zhang, S.; Yang, B.; He, C.; Xu, B.; Hou, J. Fine
36 Tuned Photoactive and Interconnection Layers for Achieving over 13% Efficiency in a
37 Fullerene-free Tandem Organic Solar Cell. *J. Am. Chem. Soc.* **2017**, *139*, 7302–7309.
38
39
40
41 (17) Wang, X.; Koleilat, G. I.; Tang, J.; Liu, H.; Kramer, I. J.; Debnath, R.; Brzozowski, L.;
42 Barkhouse, D. A. R.; Levina, L.; Hoogland, S.; et al. Tandem Colloidal Quantum Dot
43 Solar Cells Employing a Graded Recombination Layer. *Nat. Photonics* **2011**, *5*, 480-484.
44
45
46
47 (18) Choi, J. J.; Wenger, W. N.; Hoffman, R. S.; Lim, Y. F.; Luria, J.; Jasieniak, J.; Marohn,
48 J. A.; Hanrath, T. Solution-Processed Nanocrystal Quantum Dot Tandem Solar Cells.
49 *Adv. Mater.* **2011**, *23*, 3144-3148.
50
51
52
53
54
55
56
57
58
59
60

- 1
2
3 (19) Shi, G.; Wang, Y.; Liu, Z.; Han, L.; Liu, J.; Wang, Y.; Lu, K.; Chen, S.; Ling, X.; Li, Y.
4
5 Stable and Highly Efficient PbS Quantum Dot Tandem Solar Cells Employing a
6
7 Rationally Designed Recombination Layer. *Adv. Energy Mater.* **2017**, *7*, 1602667.
8
9
10 (20) Moreels, I.; Lambert, K.; Smeets, D.; De Muynck, D.; Nollet, T.; Martins, J. C.;
11
12 Vanhaecke, F.; Vantomme, A.; Delerue, C.; Allan, G. Size-Dependent Optical Properties
13
14 of Colloidal PbS Quantum Dots. *ACS Nano* **2009**, *3*, 3023-3030.
15
16
17 (21) Speirs, M.; Groeneveld, B.; Protesescu, L.; Piliago, C.; Kovalenko, M.; Loi, M. Hybrid
18
19 Inorganic–Organic Tandem Solar Cells for Broad Absorption of The Solar Spectrum.
20
21 *Phys. Chem. Chem. Phys.* **2014**, *16*, 7672-7676.
22
23
24 (22) Kim, T.; Gao, Y.; Hu, H.; Yan, B.; Ning, Z.; Jagadamma, L. K.; Zhao, K.; Kirmani, A.
25
26 R.; Eid, J.; Adachi, M. M.; et al. Hybrid Tandem Solar Cells With Depleted-
27
28 Heterojunction Quantum Dot and Polymer Bulk Heterojunction Subcells. *Nano Energy*
29
30 **2015**, *17*, 196-205.
31
32
33 (23) Aqoma, H.; Azmi, R.; Oh, S.-H.; Jang, S.-Y. Solution-Processed Colloidal Quantum
34
35 Dot/Organic Hybrid Tandem Photovoltaic Devices with 8.3% Efficiency. *Nano Energy*
36
37 **2017**, *31*, 403-409.
38
39
40 (24) Tong, J.; Yang, X.; Xu, Y.; Li, W.; Tang, J.; Song, H.; Zhou, Y. Efficient Top-Illuminated
41
42 Organic-Quantum Dots Hybrid Tandem Solar Cells with Complementary Absorption.
43
44 *ACS Photonics* **2017**, *4*, 1172-1177.
45
46
47 (25) Kim, T.; Palmiano, E.; Liang, R.-Z.; Hu, H.; Murali, B.; Kirmani, A. R.; Firdaus, Y.;
48
49 Gao, Y.; Sheikh, A.; Yuan, M.; et al. Hybrid Tandem Quantum Dot/Organic Photovoltaic
50
51 Cells with Complementary Near Infrared Absorption. *Appl. Phys. Lett.* **2017**, *110*,
52
53 223903.
54
55
56 (26) Li, Y.-L.; Yeh, P.-N.; Sharma, S.; Chen, S.-A. Promotion of Performances of Quantum
57
58 Dot Solar Cell and its Tandem Solar Cell with Low Bandgap Polymer (PTB7-Th): PC₇₁
59
60

- 1
2
3 BM by Water Vapor Treatment on Quantum Dot Layer on its Surface. *J. Mater. Chem.*
4
5 *A* **2017**, *5*, 21528-21535.
6
7
8 (27) Pattantyus-Abraham, A. G.; Kramer, I. J.; Barkhouse, A. R.; Wang, X.; Konstantatos, G.;
9
10 Debnath, R.; Levina, L.; Raabe, I.; Nazeeruddin, M. K.; Grätzel, M. Depleted-
11
12 Heterojunction Colloidal Quantum Dot Solar Cells. *ACS Nano* **2010**, *4*, 3374-3380.
13
14 (28) Barkhouse, D. A. R.; Kramer, I. J.; Wang, X.; Sargent, E. H. Dead Zones in Colloidal
15
16 Quantum Dot Photovoltaics: Evidence and Implications. *Opt. Express* **2010**, *18*, A451-
17
18 A457.
19
20 (29) He, Z.; Zhong, C.; Su, S.; Xu, M.; Wu, H.; Cao, Y. Enhanced Power-Conversion
21
22 Efficiency in Polymer Solar Cells using an Inverted Device Structure. *Nat. Photonics*
23
24 **2012**, *6*, 591-595.
25
26
27 (30) Lu, L.; Yu, L. Understanding Low Bandgap Polymer PTB7 and Optimizing Polymer
28
29 Solar Cells Based on It. *Adv. Mater.* **2014**, *26*, 4413-4430.
30
31
32 (31) Foster, S.; Deledalle, F.; Mitani, A.; Kimura, T.; Kim, K. B.; Okachi, T.; Kirchartz, T.;
33
34 Oguma, J.; Miyake, K.; Durrant, J. R.; et al. Electron Collection as a Limit to
35
36 Polymer:PCBM Solar Cell Efficiency: Effect of Blend Microstructure on Carrier
37
38 Mobility and Device Performance in PTB7:PCBM. *Adv. Energy Mater.* **2014**, *4*,
39
40 1400311.
41
42
43 (32) Ip, A. H.; Thon, S. M.; Hoogland, S.; Voznyy, O.; Zhitomirsky, D.; Debnath, R.; Levina,
44
45 L.; Rollny, L. R.; Carey, G. H.; Fischer, A.; et al. Hybrid Passivated Colloidal Quantum
46
47 Dot Solids. *Nat. Nanotechnol.* **2012**, *7*, 577-582.
48
49
50 (33) Kirmani, A. R.; Carey, G. H.; Abdelsamie, M.; Yan, B.; Cha, D.; Rollny, L. R.; Cui, X.;
51
52 Sargent, E. H.; Amassian, A. Effect of Solvent Environment on Colloidal-Quantum-Dot
53
54 Solar-Cell Manufacturability and Performance. *Adv. Mater.* **2014**, *26*, 4717-4723.
55
56
57
58
59
60

- 1
2
3 (34) Zhao, K.; Wodo, O.; Ren, D.; Khan, H. U.; Niazi, M. R.; Hu, H.; Abdelsamie, M.; Li, R.;
4
5 Li, E. Q.; Yu, L.; et al. Vertical Phase Separation in Small Molecule:Polymer Blend
6
7 Organic Thin Film Transistors Can Be Dynamically Controlled. *Adv. Funct. Mater.*
8
9 **2016**, *26*, 1737-1746.
- 10
11
12 (35) Derue, L.; Dautel, O.; Tournebize, A.; Drees, M.; Pan, H.; Berthumeyrie, S.; Pavageau,
13
14 B.; Cloutet, E.; Chambon, S.; Hirsch, L. Thermal Stabilisation of Polymer–Fullerene
15
16 Bulk Heterojunction Morphology for Efficient Photovoltaic Solar Cells. *Adv. Mater.*
17
18 **2014**, *26*, 5831-5838.
- 19
20
21 (36) Diroll, B. T.; Ma, X.; Wu, Y.; Murray, C. B. Anisotropic Cracking of Nanocrystal
22
23 Superlattices. *Nano Lett.* **2017**, *17*, 6501-6506.
- 24
25
26 (37) Jagadamma, L. K.; Abdelsamie, M.; El Labban, A.; Aresu, E.; Ndjawa, G. O. N.; Anjum,
27
28 D. H.; Cha, D.; Beaujuge, P. M.; Amassian, A. Efficient Inverted Bulk-Heterojunction
29
30 Solar Cells from Low-Temperature Processing of Amorphous ZnO Buffer Layers. *J.*
31
32 *Mater. Chem. A* **2014**, *2*, 13321-13331.
- 33
34
35 (38) Jagadamma, L. K.; Al-Senani, M.; El-Labban, A.; Gereige, I.; Ndjawa, N.; Guy, O.;
36
37 Faria, J. C.; Kim, T.; Zhao, K.; Cruciani, F.; et al. Polymer Solar Cells with Efficiency
38
39 >10% Enabled via a Facile Solution-Processed Al-Doped ZnO Electron Transporting
40
41 Layer. *Adv. Energy Mater.* **2015**, *5*, 1500204.
- 42
43
44 (39) Mali, S. S.; Hong, C. K.; Inamdar, A.; Im, H.; Shim, S. E. Efficient Planar n-i-p Type
45
46 Heterojunction Flexible Perovskite Solar Cells with Sputtered TiO₂ Electron
47
48 Transporting Layers. *Nanoscale* **2017**, *9*, 3095-3104.
- 49
50
51 (40) Kim, T.-S.; Na, S.-I.; Oh, S.-H.; Kang, R.; Yu, B.-K.; Yeo, J.-S.; Lee, J.; Kim, D.-Y. All-
52
53 Solution-Processed ITO-Free Polymer Solar Cells Fabricated on Copper Sheets. *Solar*
54
55 *Energy Mater. Sol. Cells* **2012**, *98*, 168-171.
- 56
57
58
59
60

- 1
2
3 (41) Schmidt, H.; Flügge, H.; Winkler, T.; Bülow, T.; Riedl, T.; Kowalsky, W. Efficient
4 Semitransparent Inverted Organic Solar Cells with Indium Tin Oxide Top Electrode.
5 *Appl. Phys. Lett.* **2009**, *94*, 243302.
6
7
8
9
10 (42) Gupta, D.; Wienk, M. M.; Janssen, R. A. Indium Tin Oxide-Free Tandem Polymer Solar
11 Cells on Opaque Substrates with Top Illumination. *ACS appl. Mater. Interfaces* **2014**, *6*,
12 13937-13944.
13
14
15
16 (43) Zheng, Z.; Zhang, S.; Zhang, M.; Zhao, K.; Ye, L.; Chen, Y.; Yang, B.; Hou, J. Highly
17 Efficient Tandem Polymer Solar Cells with a Photovoltaic Response in the Visible Light
18 Range. *Adv. Mater.* **2015**, *27*, 1189-1194.
19
20
21
22
23 (44) Martínez-Otero, A.; Liu, Q.; Mantilla-Perez, P.; Bajo, M. M.; Martorell, J. An Extremely
24 Thin and Robust Interconnecting Layer Providing 76% Fill Factor in a Tandem Polymer
25 Solar Cell Architecture. *J. Mater. Chem. A* **2015**, *3*, 10681-10686.
26
27
28
29
30 (45) Guyot-Sionnest, P. Electrical Transport in Colloidal Quantum Dot Films. *J. Phys.*
31 *Chem. Lett.* **2012**, *3*, 1169-1175.
32
33
34
35
36
37
38
39
40
41
42
43
44
45
46
47
48
49
50
51
52
53
54
55
56
57
58
59
60